30.0 MECHANISMS OF GRAIN REFINEMENT IN LASER POWDER BED FUSION OF IN-SITU METAL MATRIX COMPOSITE 6061 ALUMINUM ALLOYS

Chloe Johnson (Mines)
Faculty: Amy Clarke (Mines)
Industrial Mentors: Paul Wilson (Boeing), John Carpenter (LANL), and Jeremy Iten (Elementum 3D)

30.1 Project Overview and Industrial Relevance

The advent of additive manufacturing (AM) has allowed for the design and production of near net shape components, as well as the incorporation of complex internal networks (*e.g.* cooling channels or lattices) inside of parts by 3D printing. Despite these advantages the number of printable alloys is currently limited, due to the solidification conditions experienced during AM, which can lead to large columnar grains, resulting in potential anisotropic behavior in the final part. Defects such as hot cracking, caused by shrinkage of solute-rich liquid between dendrites in the final stages of solidification, can also occur due to a large solidification temperature range. These effects are exacerbated in Al alloys, due to their high thermal conductivity, which increases the thermal gradient (G), and tendency to have a large "mushy zone", or region where solid and liquid coexist, and thus a large solidification temperature range [30.1]. A few strategies have been suggested to address these issues, primarily focusing on grain refinement via alloying and/or inoculation, or reducing G and modifying the solid-liquid velocity (V) via process parameters to induce the columnar to equiaxed transition (CET). While most laser powder bed fusion (LPB-F) studies have focused on alloying or optimizing laser parameters, the former limits the number of alloys that can be used, while the latter can still lead to columnar growth [30.1, 30.2]. A promising option of inoculating Al alloys to induce grain refinement has been shown to produce a refined equiaxed microstructure free of solidification cracking that achieves good mechanical properties [30.3]. However, studies on inoculated Al alloys are limited, and mostly focus on proof of concept, rather than identifying specific grain refinement mechanisms. This study proposes to investigate grain refinement mechanisms in inoculated A6061-RAM (reactive additive manufacturing) alloys developed and designed for AM by Elementum 3D. These alloys contain micron-scale additive powders that dissolve in the melt, undergo a thermodynamically favorable reaction, and form submicron-scale particles that serve as inoculants to refine the microstructure. Additionally, some of the additive reactant powders do not fully dissolve during processing. In combination with finer, inoculant product particles, they serve to effectively create a metal matrix composite (MMC) with improved mechanical performance. *In-situ* and ex-situ microstructural characterization techniques will be used to understand grain refinement mechanisms in A6061-RAM alloys, which will add to the variety of inoculated Al alloys for potential use under AM conditions, as well as help to inform fundamental understanding of grain refinement mechanisms in these alloys.

30.2 Previous Work

Initial microscopy of A6061-RAM2 and the powder feedstock, where the "2" refers to the amount of added reactant particles in volume percent, has been performed to reveal the two additive powders (white and black in the SEM image) on the scale of ~1-10 microns (**Figure 30.1**). These particles are smaller than the starting alloy powder (grey in the SEM image), shown to be on the scale of tens of microns. Two types of particles can be observed in the 6061 matrix after the build process. The first is incompletely dissolved reactant particles in the matrix, up to a few microns in size. The second is fine, submicron sized particles in the matrix, attributed to the product of inoculant particles formed in the melt during the printing process. Both types of particles are potential nucleation sites and contribute to strengthening of the MMC.

In-situ solidification experiments were performed in March 2019 and February 2020 using the LPB-F AM simulator at the Advanced Photon Source (APS) at Argonne National Laboratory (ANL) (**Figure 30.2**) [30.4]. These experiments allow for *in-situ* X-ray imaging of a laser raster or spot melt formed by selected parameters on plate, powder, or plate with powder samples. For samples containing powder, glassy carbon plates are situated on either

side of the sample to contain the powder and control the powder layer thickness, based on the height of both the base plate and the glassy carbon. The radiography data captured in these experiments allow for the determination of solidification velocity (V), which can then be correlated to specific observations in the microstructure of the melt pool to better understand how solidification conditions impact microstructural development. Wrought 6061 and A6061-RAM AM builds were used as base plates and coupled with 6061, A6061-RAM2, or A6061-RAM10 powders to consider the impact of varying RAM contents on the microstructure for different solidification conditions. To consider a wide variety of AM parameters for each of the material sets outlined in **Table 30.1**, laser parameters (given in **Table 30.2**) were selected by generating a G-V map using the Rosenthal equation [30.5] and by considering bounds determined from experience with previous experiments.

30.3   Recent Progress

30.3.1   Effect of Solidification Conditions on Grain Refinement

The in-situ experiments performed using the AM simulator at the APS allow for direct correlation of solidification conditions (specifically Vs) to the post-mortem microstructure. As stated before, the base plate materials used for these experiments (given in **Table 30.1**) consisted of either wrought 6061, A6061-RAM2, or A6061-RAM2, with a powder layer corresponding to one of the RAM powders, or conventional 6061 powder. Example microstructures of the wrought 6061 base plate and a raster performed on a wrought 6061 base plate/6061 powder sample using the in-situ AM simulator are shown by electron back scatter diffraction (EBSD) inverse pole figure maps (IPFs) (**Figure 30.3**). Despite the mostly equiaxed microstructure of the wrought baseplate, both cracking and columnar grains following the build direction can be seen in the sample generated using the AM simulator (**Figure 30.3b-c**). This is in stark contrast compared to the refined equiaxed microstructure observed in the samples consisting of a A6061-RAM base plate and powder layer (**Figure 30.4**). While multiple studies have been performed on the impact of various solidification conditions on the final microstructure of 6061 parts built using AM [30.6], this has yet to be evaluated for A6061-RAM alloys. The average grain size (**Table 30.3**), alongside example EBSD IPFs of the observed microstructures (**Figure 30.4**) from sample sets consisting of either a base plate of A6061-RAM2 with a A6061-RAM2 powder layer, or A6061-RAM10 with a A6061-RAM10 powder layer, imply the refinement achieved in these alloys is seemingly more dependent upon RAM additions than the range of solidification conditions used in the experiments performed and characterized to date. This average grain size was measured using MTEX software, defining grain boundaries based on a 5-degree misorientation angle. Grain area was used to account for any effect of aspect ratio or non-equiaxed morphology on grain size. EBSD IPFs were processed using neighbor patterning and averaging reindexing (NPAR) and neighbor orientation correlation through OIM analysis software.

Samples consisting of a base plate of wrought 6061 with a powder layer of either A6061-RAM2 or A6061-RAM10 were also investigated to see if refined grains could be observed with less powder or incomplete mixing of reactant particles. Investigation of these "hybrid" samples containing an A6061-RAM10 layer has revealed a range of grain sizes and morphologies based on melt pool location. However, the location of grain morphology and size transition does not appear to correlate to regions typically associated with columnar to equiaxed transition, for example, seen during solidification of a conventional alloy. Rather, regions of transition in grain morphology and size appear to correlate directly to the solute or particles observed in that region. This can be seen in the scanning electron microscope (SEM) images and EBSD IPFs taken from selected samples (**Figure 30.5**). While exact grain size range, melt pool morphology, and grain size and morphology transition region vary for different conditions, similar microstructural features are observed. Despite the range in grain sizes observed throughout the melt pool, the average grain size in these samples is not far off of those observed in samples consisting of an A6061-RAM build plate with a layer of A6061-RAM powder (**Table 30.3**). Further characterization will be performed on the hybrid samples containing an A6061-RAM2 powder layer.

30.3.2   Reactive Particle Dissolution and Products

If solute distribution and/or particle formation are the main contributors to refinement in these alloys, the formation and state of particle types during melting and solidification and the contribution to refinement in the microstructure needs to be explored. This could largely depend upon the amount of reactant particles in the starting material, as well as the amount of these particles that dissolve. Investigation of the types of particles that could be formed in

these alloys began with CALPHAD predictions using Thermo-Calc Scheil solidification modeling, performed with the assumption that reactant particles were fully dissolved into a pure Al liquid, considering a temperature range of 25-3000°C. The results of these simulations for 0.5, 1, 2, and 10 vol. % reactant particle concentrations are shown in **Figure 30.6** and **Table 30.4**. A wide variety of particles are predicted to form, with only volume fraction of particles changing between 0.5-2 vol. %, while additional particle species are predicted to form in the 10 vol. % samples.

Microstructural characterization of particle formation in these alloys has begun with consideration of samples containing 10 vol. % of reactant particles; samples containing 0.5, 1, and 2 vol. % will be considered in future work. Recent experimental observations of these microstructures (**Figure 30.7**) have been performed using SEM and energy dispersive spectroscopy (EDS). **Figure 30.7a-b** show EDS mapping performed around two partially dissolved reactant particles from an as-built sample, the first being a boron carbide (B_4C) particle and the second a titanium (Ti) particle. According to literature, boron (B) and especially carbon (C) diffuse much faster in Al than Ti [30.7], which could lead to the formation of a Ti depleted region around the B_4C particle, as these species would diffuse away from the B_4C and react to form products with Ti further away from the source particle. In this Ti poor region, there still appears to be Al-rich phases that form, which could potentially be Al carbides or borides. The Ti particle in **Figure 30.7b** appears to have a layer of another phase surrounding it. EDS suggests this layer to be a Ti-rich phase that could contain some B or C. It is important to note, however, that while EDS provides valuable information regarding Ti and Al in the microstructure, it is qualitative in regards to the presence of B and C, and thus no firm conclusions as to the phase of this layer can be made with currently available information. The complexity of what is observed in these alloys (**Figure 30.7c**) shows a wide variety of phases that could be forming around Ti and B_4C particles near each other. EDS of part of this area (**Figure 30.7d**) gives some insight into what regions are more Ti versus Al rich, but exact identification of these particles will require more in-depth analysis using techniques such as x-ray diffraction, electron probe microanalysis or transmission electron microscopy.

30.4   Plans for Next Reporting Period

The plans for next reporting period include:
- Complete investigation of the effect of solidification conditions on grain refinement in RAM alloys in remaining APS samples.
- Investigate the impact of various RAM contents on final microstructure in AM builds of RAM 0.5%, 1%, 2%, and 10%, as well as the various phases that form due to the RAM reaction.
- Evaluate the impact of RAM particles on heat treatment behavior in A6061-RAM alloys.

30.5   References

[30.1]   J. Zhang, B. Song, Q. Wei, D. Bourell, Y. Shi, A Review of SLM of Aluminum Alloys: Processing, Microstructure, Property, and Developing Trends, Journal of Materials Science and Technology. 35 (2019) 270-284.

[30.2]   D. Buchbinder, W. Meiners, K. Wissenbach, R. Poprawe, Selective Laser Melting of Aluminum Die-Cast Alloy-Correlations Between Process Parameters, Solidification Conditions, and Resulting Mechanical Properties, Journal of Laser Applications. 27 (2015) 1-6.

[30.3]   J. H. Martin, B. D. Yahata, J. M. Hundley, J. A. Mayer, T. A. Schaedler, T. M. Pollock, 3-D Printing of High-Strength Aluminium Alloys, Nature. 549 (2017) 303-314.

[30.4]   C. Zhao, K. Fezzaa, R. Cunningham, H. Wen, F. De Carlo, L. Chen, A.D. Rollett, T. Sun, Real-Time Monitoring of Laser Powder Bed Fusion Process Using High-Speed X-Ray Imaging and Diffraction, Scientific Reports. 7 (2017) 1-11.

[30.5]   A. Plotkowski, M.M. Kirka, S.S. Babu, Verification and Validation of Rapid Heat Transfer Calculation Methodology for Transient Melt Pool Solidification Conditions in Powder Bed Metal Additive Manufacturing, Additive Manufacturing. 18 (2017) 256-268.

[30.6]   S. Z. Uddin, L. E. Murr, C. A. Terrazas, P. Morton, D. A. Roberson, R. B. Wicker, Processing and Characterization of Crack-Free Aluminum 6061 Using High-Temperature Heating in Laser Powder Bed Fusion Additive Manufacturing, Additive Manufacturing. 22 (2018) 405-415.

[30.7]   B. Zou, P. Shen, Q. Jiang, Reaction Synthesis of $TiC-TiB_2$/Al Composites from an $Al-Ti-B_4C$ System, Journal of Materials Science. 42 (2007) 9927-9933.
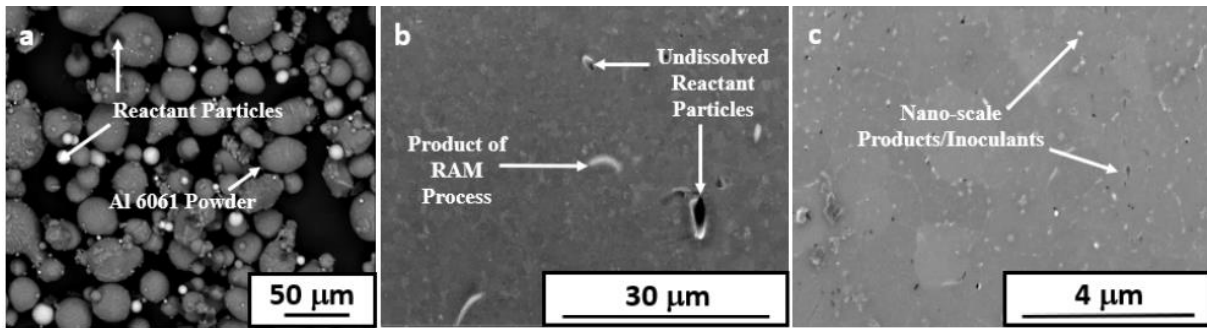
30.6   Figures and Tables

Figure 30.1: Backscattered electron SEM images of a) the 6061 RAM with 2% inoculant powder feedstock and b) the general microstructure of an as-built cube after the laser powder bed fusion build process. The arrows show initial and unreacted inoculant powders before and after the build process. c) A secondary electron SEM image of the submicron-size products/inoculants from the RAM process, which can be seen in and around the grains.

Table 30.1: Material sets for in-situ experiments performed at the APS. The base plate consisted of material that was 3 mm in height, 50 mm in length, and ~0.75 mm in thickness. Powder size (as seen in the last image) was in the range of 1-60 μm.

Base Plate Material	Powder Layer Material
6061 Wrought	6061
6061 Wrought	A6061-RAM2
6061 Wrought	A6061-RAM10
A6061-RAM2	A6061-RAM2
A6061-RAM10	A6061-RAM10

Table 30.2: Laser parameters chosen for samples tested at APS in February 2020, corresponding to data presented in this report.

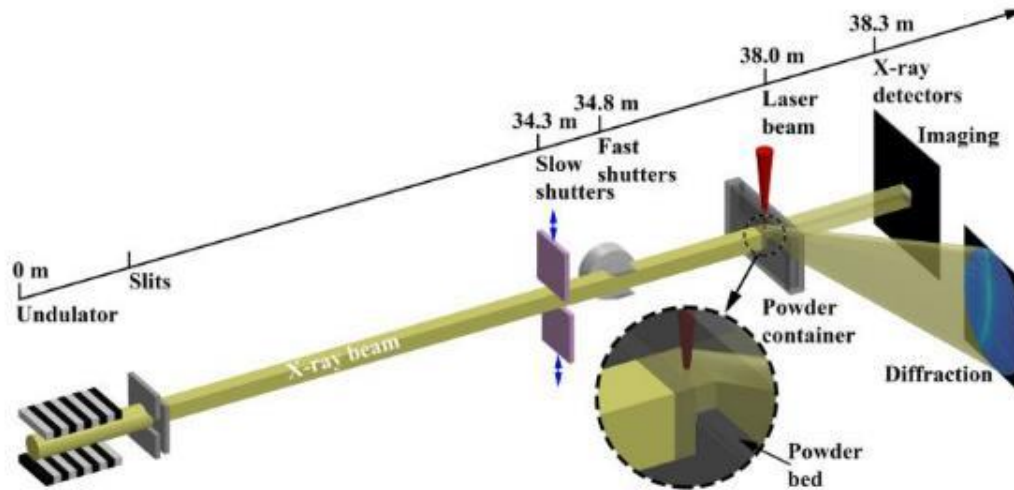| Laser Power (W)	Laser Speed (m/s)
311	0.5
397	1
397	1.5
540	1.5
540	2

Figure 30.2: Schematic of the AM simulator at Sector 32-ID of the APS. A sample (powder, powder on plate, or plate) is loaded into a sample chamber backfilled with argon gas. A programmable laser then performs either a raster or single melt spots on the sample in the chamber, while the x-rays transmit through this chamber. This produces radiographic images of the melt pool *in-situ* for tracking of the solid-liquid interface, as well as giving insight into any other observed phenomena. Taken from [30.4].

31.5
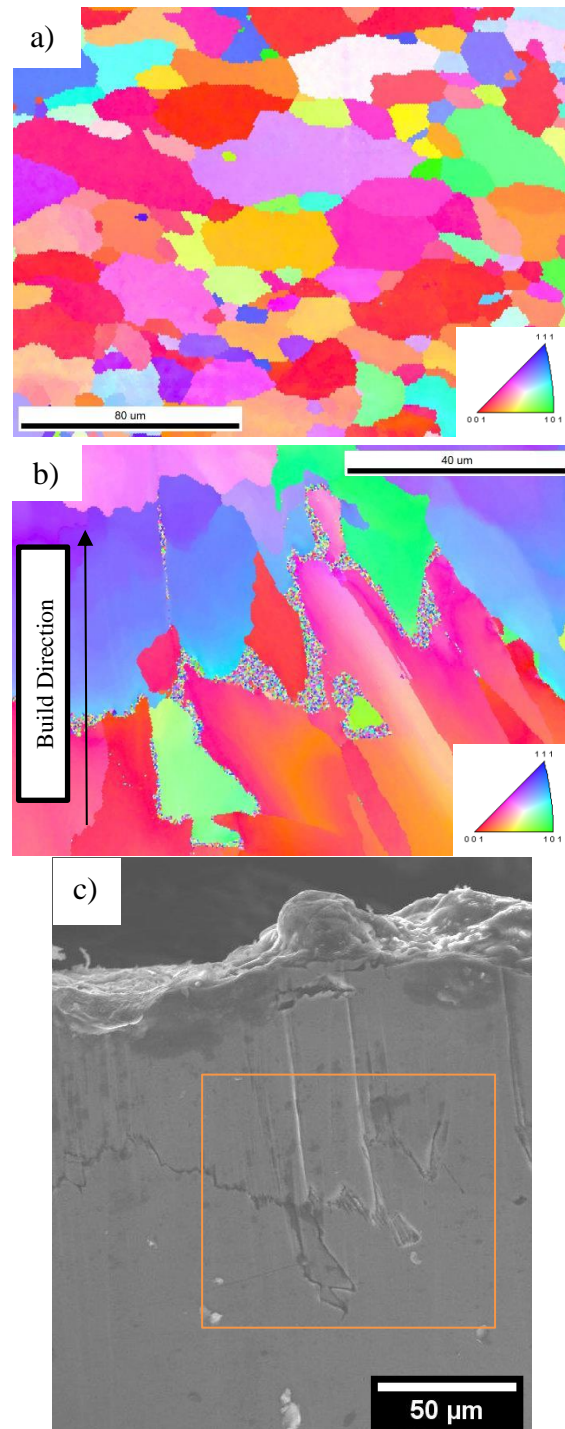
Figure 30.3: EBSD IPF maps of a) a wrought 6061 base plate, taken from a location in a wrought 6061 base plate away from the melt pool shown in b) which was taken from a raster on a 6061 wrought base plate with a 6061 powder layer performed using the AM simulator at APS. The IPF shown in b) corresponds to the region shown in c) bounded by the orange box, taken from the steady state region of the raster. This raster was performed with a laser power and speed of 426 W and 0.5 m/s, respectively. c) Also, a crack is captured by the speckled region (indicative of low confidence index) of the IPF. This crack is an example of solidification cracking that typically occurs in AM of stock aluminum alloys.

31.6

Table 30.3: Average grain size of investigated material sets determined using MTEX software. Grains were defined by regions with a misorientation angle of 5 degrees. Area was used to capture any effects of aspect ratio on grain size.

Sample Number	Laser Power (W)	Laser Speed (m/s)	Linear Energy Density (J/m)	Average Grain Area (μm^2)		
				RAM2 base/RAM2 powder	RAM10 base/RAM10 powder	Wrought 6061 base/RAM10 powder
1	311	0.5	622	0.91	0.49	0.48
2	397	1	397	0.83	0.53	-
3	397	1.5	265	0.95	0.27	1.22
4	540	1.5	360	0.84	0.38	0.67
5	540	2	270	0.72	0.19	0.39
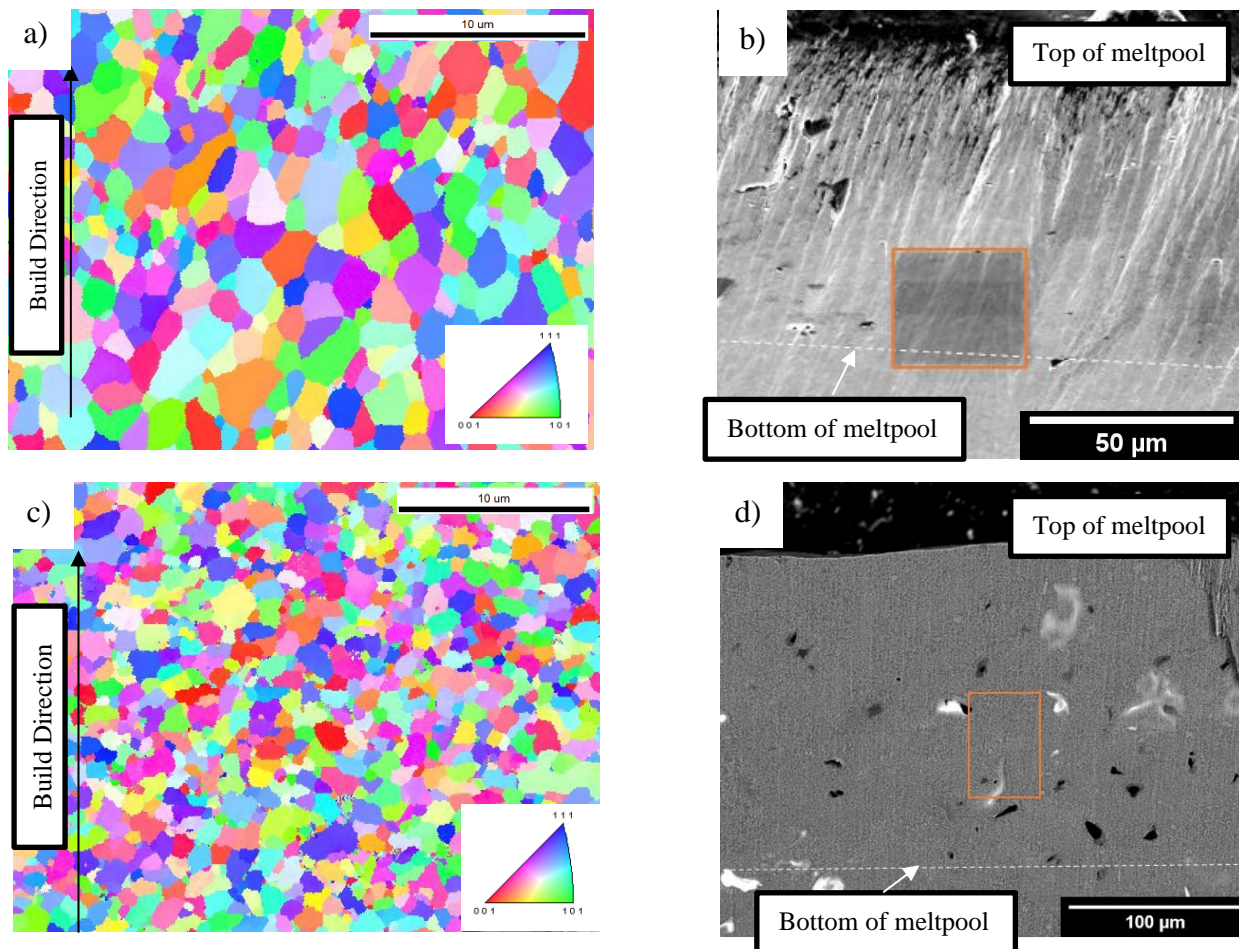
Figure 30.4: EBSD IPF maps of a) an A6061-RAM2 AM build base plate with an A6061-RAM2 powder layer and c) an A6061-RAM10 AM build base plate with an A6061-RAM10 powder layer made using the AM simulator at APS. The location of both IPF maps are shown in the corresponding images in b) for a) and d) for c), with the orange box corresponding to the IPF map location. These maps were taken in the steady-state region of a raster, with both rasters performed with a laser power and speed of 311 W and 0.5 m/s, respectively. Both scans are representative of the morphology and grain size observed for a variety of solidification conditions within the same material set.
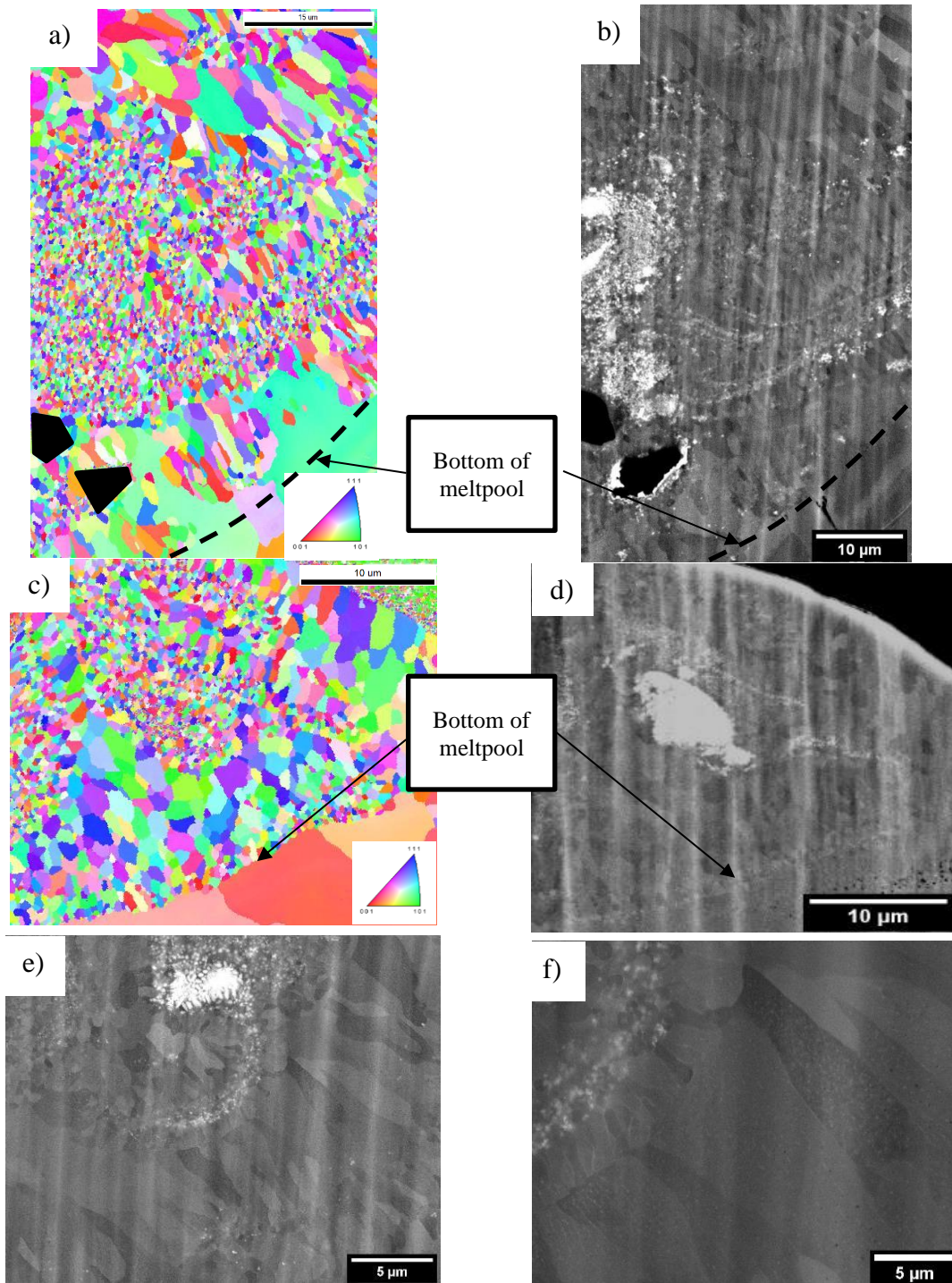
31.7

Figure 30.5: a) and c) EBSD IPF maps of a raster performed on a sample consisting of a base plate of 6061with a powder layer of A6061-RAM10: a) was taken at the termination of a raster, which was performed with laser settings of 540 W and 2 m/s, while c) was taken in the steady-state (near middle along the length) region of a raster performed with laser settings of 397 W and 1.5 m/s. For both regions the top of the scan corresponds to the top of the melt pool. b) and d) are corresponding SEM back scatter electron (BSE) images corresponding to the same regions shown in a) and c) respectively. e) and f) show high magnification SEM BSE images of an area with larger grains and finer grains, highlighting the particles and/or solute-rich areas in these regions.
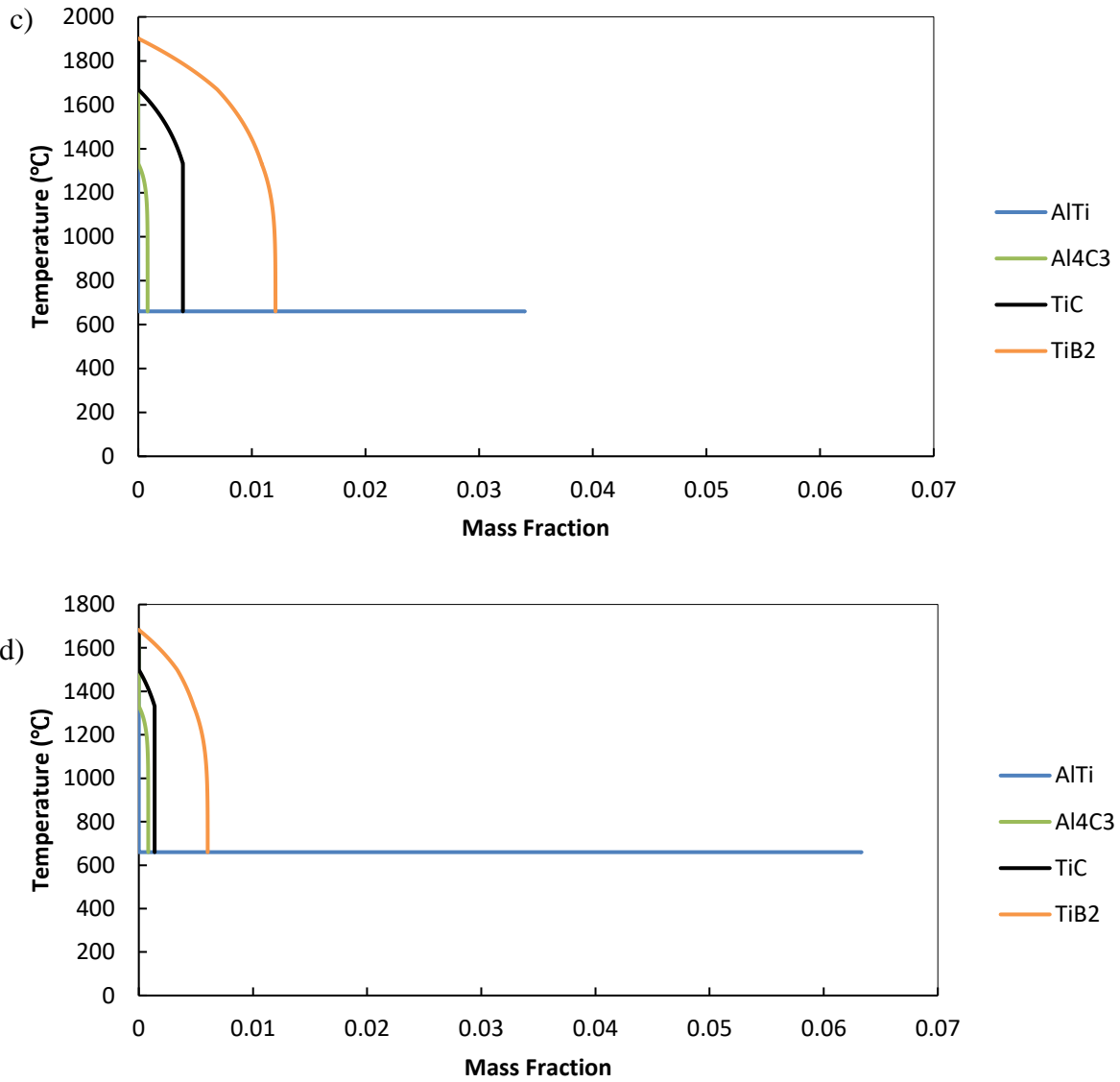
31.8

a)

b)
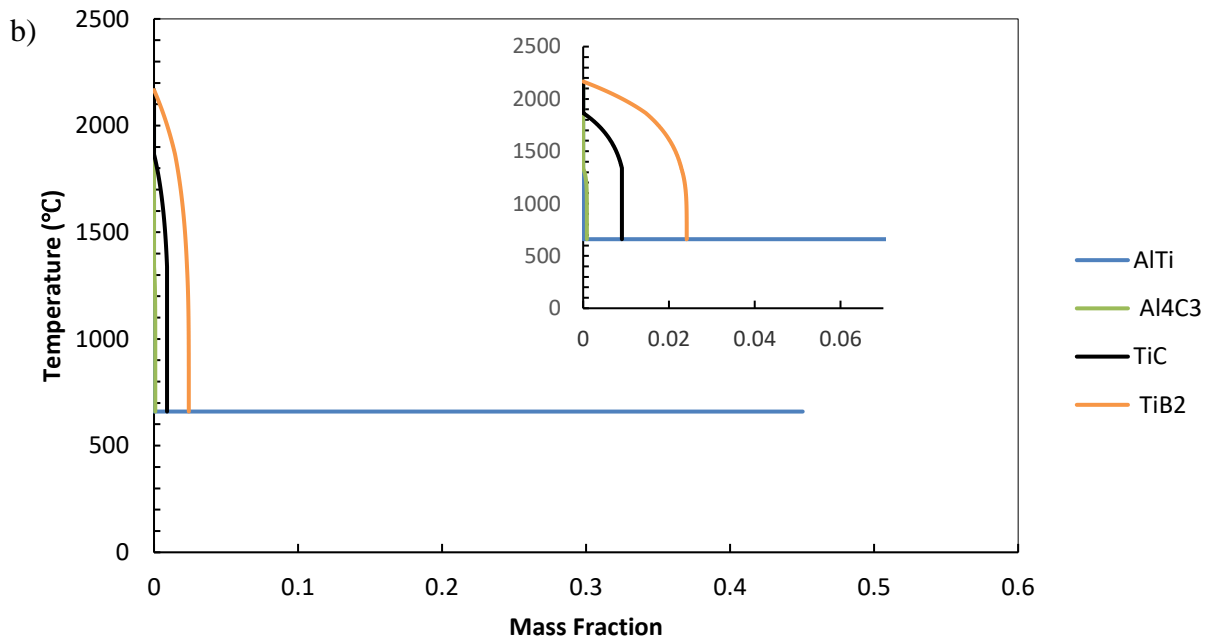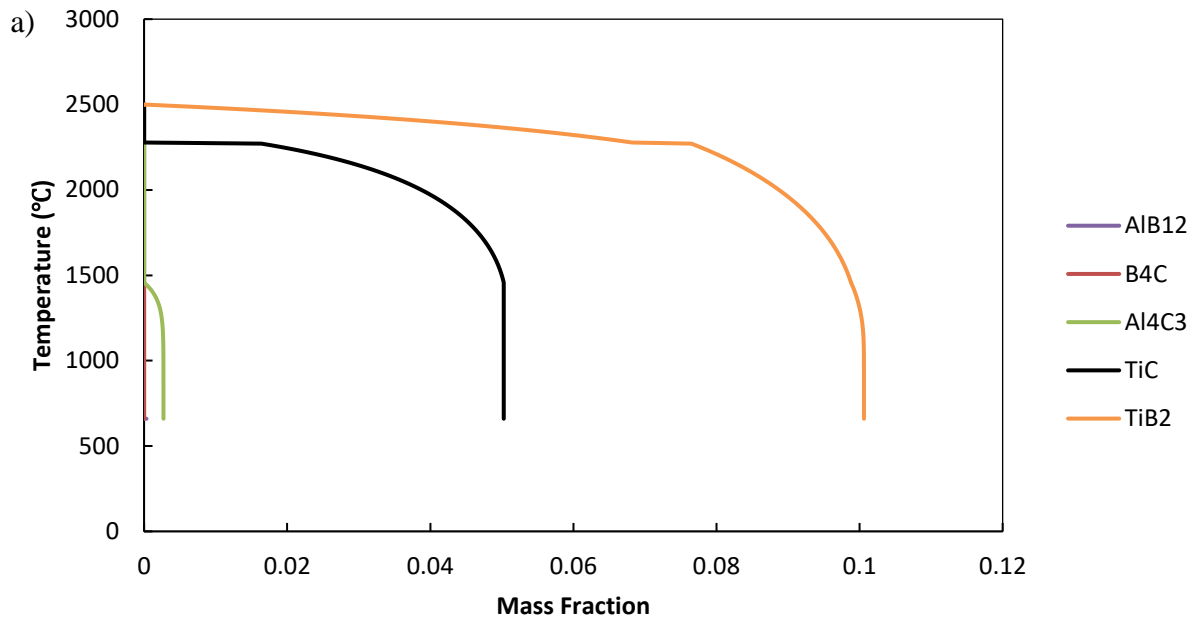
Figure 30.6: Mass fractions of predicted phases based on Scheil solidification modeling using Thermo-Calc software for various starting reactive particle amounts: a) 10, b) 2, c) 1, and d) 0.5 vol. %, assuming reactant particles completely dissolved in pure liquid Al, over a temperature range of room temperature to 3000°C.

31.10

Table 30.4: Mass fractions of predicted phases based on Scheil solidification modeling using Thermo-Calc. Existence of these particles in the material, and their effect on final microstructure, has yet to be evaluated.

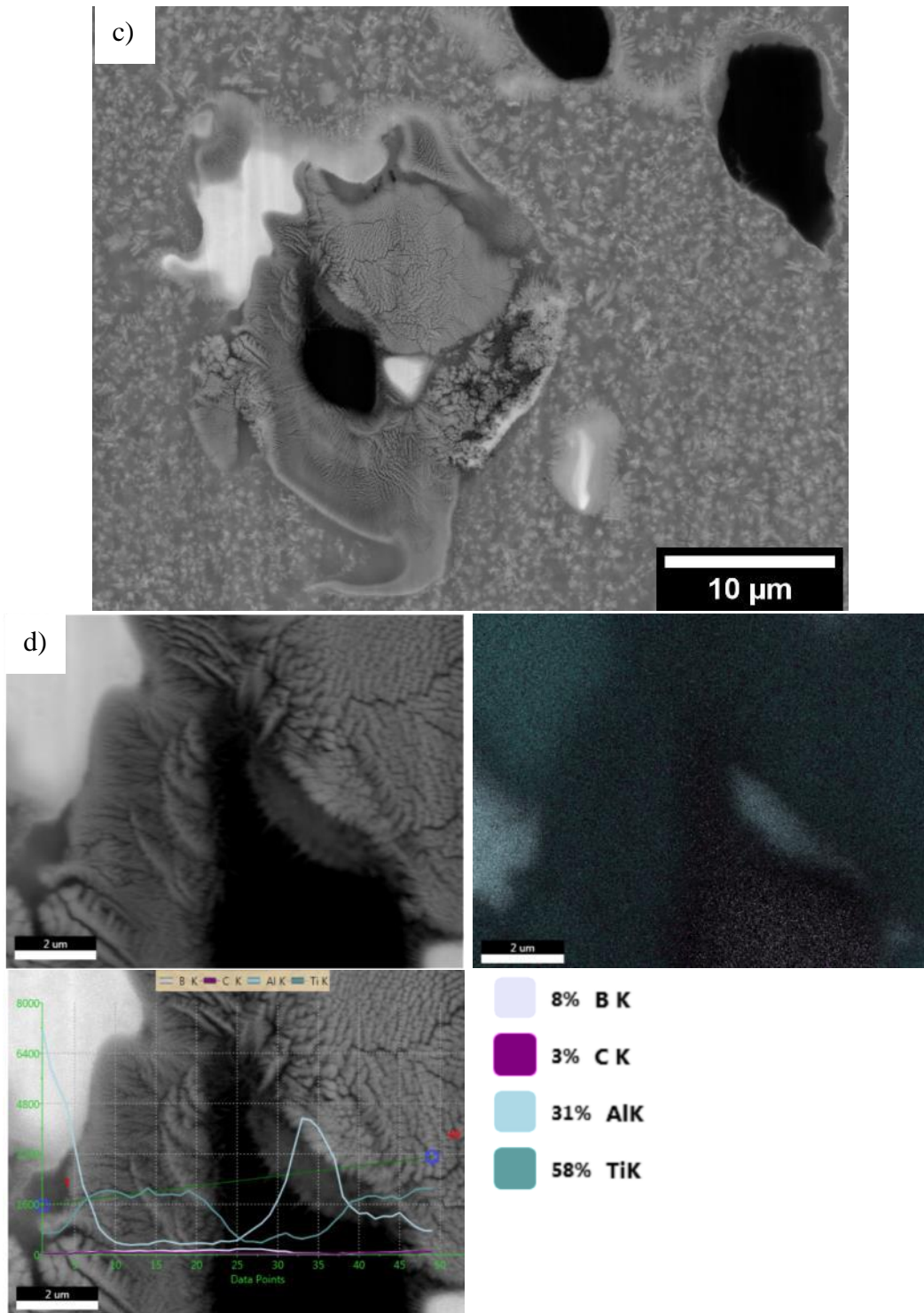| Phase	Mass Fraction of Phase at end of Solidification			
	RAM 10%	RAM 2%	RAM 1%	RAM 0.5%
AlTi	-	0.45	0.034	0.063
Al4C3	0.0027	0.00087	0.00082	0.00083
TiC	0.05	0.009	0.0039	0.0014
TiB2	0.1	0.024	0.012	0.006
AlB12	0.00034	-	-	-
B4C	1.11e-7	-	-	-

31.11
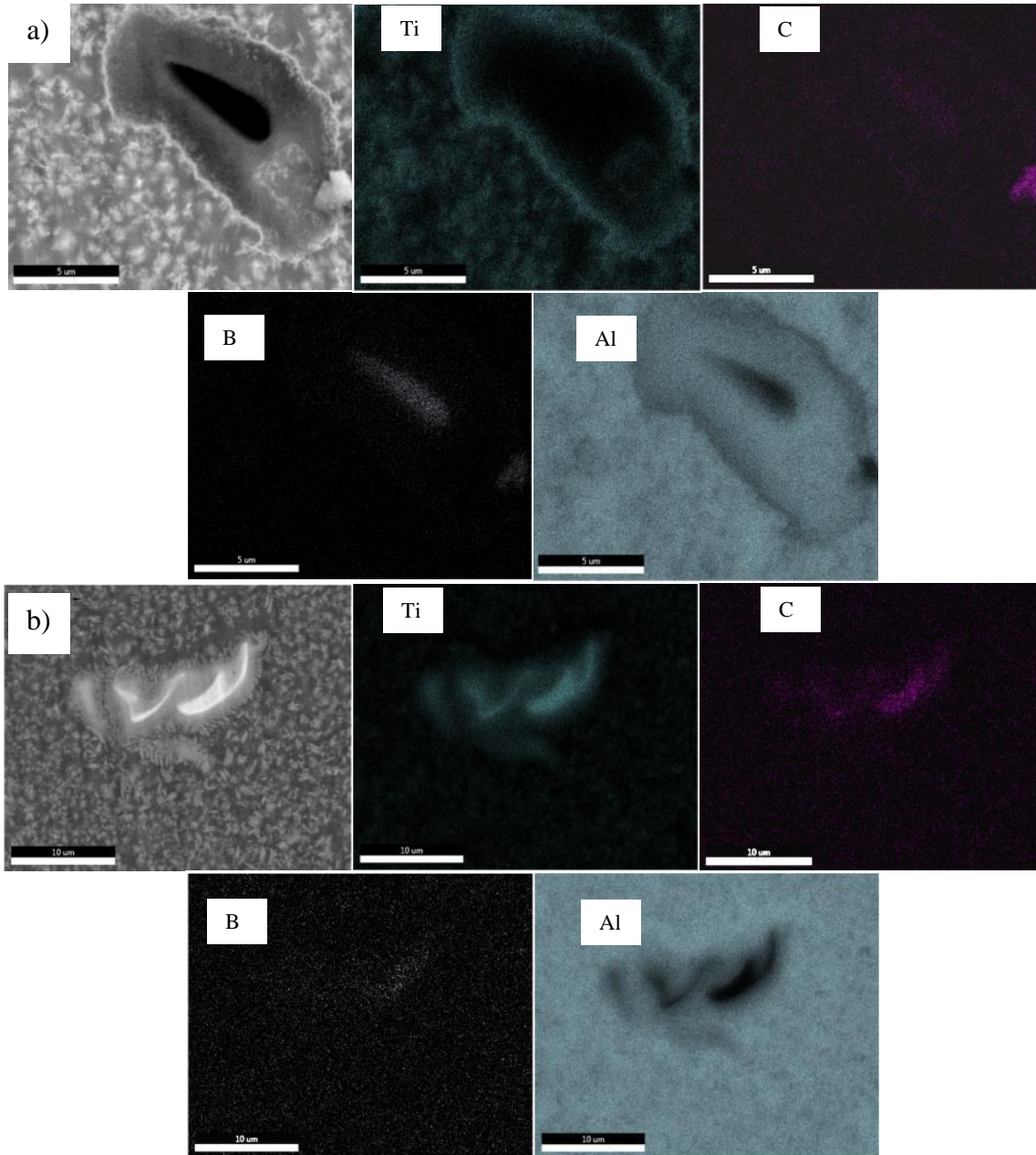
Figure 30.7: a), b) & d) EDS mapping of various particles and phases in a A6061-RAM10 alloy AM build. a) and b) show areas around two undissolved reactive particles, namely B_4C and Ti, respectively. c) and d) show an example of the wide range of particles that can form when these particles react.

31.12